Estimating the concentration of aluminum-substituted hematite and goethite using diffuse reflectance spectrometry and rock magnetism: feasibility and limitations

Pengxiang Hu[1, 2, 3], Zhaoxia Jiang[1], Qingsong Liu[1, 4, *], David Heslop[3], Andrew P. Roberts[3], José Torrent[5], Vidal Barrón[5]

[1] Division of Tethys Research Center, Institute of Geology and Geophysics, Chinese Academy of Sciences, Beijing 100029, China

[2] University of the Chinese Academy of Sciences, Beijing 100049, China

[3] Research School of Earth Sciences, The Australian National University, Canberra, ACT 2601, Australia

[4] Laboratory for Marine Geology, Qingdao National Oceanography Laboratory for Science and Technology, Qingdao, China

[5] Departamento de Agronomía, Universidad de Córdoba, 14071 Córdoba, Spain

*Corresponding author: Qingsong Liu

Institute of Geology and Geophysics, Chinese Academy of Sciences,

No. 19, Beitucheng Western Road, Chaoyang District, 100029, Beijing, China

E-mail: qsliu@mail.iggcas.ac.cn

Tel: +86-10-82998365

Fax: +86-10-62010846

This article has been accepted for publication and undergone full peer review but has not been through the copyediting, typesetting, pagination and proofreading process which may lead to differences between this version and the Version of Record. Please cite this article as doi: 10.1002/2015JB012635

Key points

Synthetic Al-hematite/goethite is used to estimate concentrations by DRS and HIRM

New relations between DRS and concentration ratio of goethite to hematite are derived

DRS and HIRM can be used to quantify hematite and goethite in Chinese loess sequences

Abstract Hematite and goethite in soils are often aluminum (Al) substituted, which can dramatically change their reflectance and magnetic properties and bias abundance estimates using diffuse reflectance spectroscopy (DRS) and magnetic techniques. In this study, synthetic Al-substituted hematites and goethites, and two Chinese loess/paleosol sequences were investigated to test the feasibility and limitations of estimating Al-hematite and Al-goethite concentration. When Al substitution is limited (Al/(Al + Fe) molar ratio < ~8%), the reflectance spectrum provides a reliable estimate of the goethite/hematite concentration ratio. New empirical relationships between the DRS band intensity ratio and the true concentration goethite/hematite ratio are estimated as goethite/hematite = 1.56 × ($I_{425\ nm}/I_{535\ nm}$) or goethite/hematite = 6.32 × ($I_{480\ nm}/I_{535\ nm}$), where $I_{425\ nm}$, $I_{480\ nm}$, and $I_{535\ nm}$ are the amplitudes of DRS second-derivative curves for characteristic bands at ~425 nm, ~480 nm, and ~535 nm, respectively. High Al substitution (> ~8%) reduces DRS band intensity, which leads to biased estimates of mineral concentration. Al substitution and grain size exert a control on coercivity distributions of hematite and goethite and, thus, affect the hard isothermal remanent magnetization (HIRM). By integrating DRS and magnetic methods, we suggest a way to constrain hematite and goethite Al substitution in natural loess. Results indicate that hematite and goethite in Chinese loess have Al contents lower than ~8%, and, thus, that DRS can be used to trace hematite and goethite concentration variations.

1. Introduction

Hematite and goethite are the most commonly occurring Fe oxides in rocks and sediments [*Barrón and Montealegre,* 1986; *Cornell and Schwertmann,* 2003; *Frost,* 1991; *Hochella et al.,* 2008; *Torrent et al.,* 2007; *Walker et al.,* 1981]. They are thermodynamically stable at ambient temperatures and are often the product of weathering-induced mineral transformations [*Barrón et al.,* 2003; *Cornell and Schwertmann,* 2003; *Michel et al.,* 2010]. Goethite occurs predominantly in cool humid climates, while hematite formation is favored in warmer, subtropical and tropical climates [*Cornell and Schwertmann*, 2003; *Felix-Henningsen,* 2000; *Kämpf and Schwertmann*, 1983]. Therefore, hematite and goethite concentrations, as well as their relative abundances, have been used widely as indicators of soil moisture regime and pedogenic processes, which are in turn related to climate variability [*Balsam et al.*, 2004; *Hao et al.*, 2009; *Ji et al.*, 2004; *Long et al.*, 2011; *Lyons et al.*, 2014].

Given the environmental importance of hematite and goethite, it is essential to develop techniques to determine reliably their concentration in natural sediments. X-ray diffraction (XRD) [*Memon et al.,* 2009], Mössbauer spectroscopy [*Eyre and Dickson,* 1995], selective chemical extraction [*Hu et al.*, 2013; *Poulton and Canfield,* 2005], magnetic techniques [*Liu et al.*, 2007; *Thompson and Oldfield,* 1986], and electromagnetic spectroscopy [*Balsam et al.*, 2004, 2014; *Deaton and Balsam,* 1991; *Jiang et al.,* 2013; *Liu et al.,* 2011] have all been proposed for hematite and goethite quantification. Under optimal conditions, the detection limit for XRD analysis is 1~2 wt.% [*Deaton and Balsam*, 1991; *Memon et al.,* 2009]. In natural materials, however, both minerals typically occur with concentrations well below this limit. Mössbauer spectrometry only provides estimates of the relative proportion of Fe phases and measurements are too time consuming to allow routine analysis of large numbers of samples. Selective chemical extraction procedures cannot yet fully separate hematite from

goethite concentration [*Hu et al.*, 2013; *Poulton and Canfield*, 2005]. The 'hard' isothermal remanent magnetization (HIRM) is often employed as a semi-quantitative magnetic proxy for hematite and goethite [*Hao et al.*, 2009; *Liu et al.*, 2007; *Thompson and Oldfield*, 1986]; however, this parameter can be compromised by the presence of higher coercivity magnetite/maghemite and inherent variations in the coercivity distributions of hematite and goethite [*Liu et al.*, 2007].

Diffuse reflectance spectroscopy (DRS) provides a quantitative method to determine mass concentrations of hematite and goethite as low as ~0.01 wt.% [*Balsam et al.*, 2014; *Deaton and Balsam*, 1991; *Ji et al.*, 2002]. DRS-based quantification of hematite and goethite has been applied to marine sediments [*Zhang et al.*, 2007], Chinese loess [*Balsam et al.*, 2004; *Ji et al.*, 2001; *Torrent et al.*, 2007] and red clay [*Hao et al.*, 2009] sequences, river terrace paleosols [*Lyons et al.*, 2014], and modern soils [*Jordanova et al.*, 2013; *Long et al.*, 2011]. DRS measurements are rapid and non-destructive, and, unlike techniques such as XRD, DRS is not limited to crystalline material [*Balsam et al.*, 2005] and can be used to quantify amorphous components. Several empirical relationships have been established to estimate hematite and goethite abundance from DRS spectra. These techniques can be divided into two groups (Table A1). First, color indices, such as "redness" (Table A1), are commonly used to estimate hematite content [*Balsam et al.*, 2004, 2014; *Barrón and Torrent*, 1986; *Ji et al.*, 2001, 2002; *Long et al.*, 2011; *Torrent et al.*, 1980, 1983]. Second, derivatives of the reflectance spectra are used to quantify characteristic features due to hematite and goethite [*Deaton and Balsam*, 1991; *Jiang et al.*, 2013; *Liu et al.*, 2011; *Scheinost et al.*, 1998; *Torrent et al.*, 2007]. For this method, citrate-bicarbonate-dithionite (CBD) extractable Fe (Fe_d) is assumed as the total iron of hematite and goethite: Fe_d = hematite/1.43 + goethite/1.59 [*Torrent et al., 2007*]. Then, the hematite and goethite concentration ratio is obtained using empirical formulae based on their DRS band intensity. Most studies use a variety of natural

samples to establish empirical functions to quantify hematite and goethite. However, these relationships lack calibration based on well-quantified synthetic samples. Additionally, existing DRS-based quantification methods assume that characteristic features within reflectance spectra depend solely on hematite and goethite concentration.

Contrary to existing assumptions, the reflectance spectra of hematite and goethite can be influenced significantly by particle size [*Torrent and Barrón*, 2003, 2008] and Al substitution [*Jiang et al.*, 2013; *Liu et al.*, 2011; *Malengreau et al.*, 1997], which are often covariant [*Torrent and Barrón*, 2003]. Earlier studies have suggested that both the position and intensity of hematite and goethite DRS bands are negatively correlated with the degree of Al substitution [*Jiang et al.*, 2014a; *Liu et al.*, 2011; *Torrent and Barrón*, 2003], which indicates potential ambiguities in DRS-based hematite and goethite quantification. The ubiquity of Al in weathering environments results in most soil Fe oxides being Al-substituted [*Cornell and Schwertmann*, 2003], and the Al content of iron oxides, in turn, can potentially provide important weathering and provenance information. Therefore, it is essential to understand the influence of Al substitution on hematite and goethite quantification.

We have performed a systematic analysis of synthetic Al-hematites and Al-goethites using DRS and magnetic quantification methods. This is complemented by investigation of two Chinese loess/paleosol sequences. The aim of this study is to test the feasibility of DRS and magnetic quantification methods and to provide insights into their use to enable more robust paleoenvironmental reconstructions.

2. Samples and Methods

Synthesis procedures used to prepare all of the studied hematite and goethite specimens are summarized in Table 1. HFh* and HGL* are hematites and GT* are goethites. Specimen numbers correspond to the initial Al content (Al/(Fe + Al) mol%). More detailed information

for the HFh* and HGL* hematite series has been reported by *Jiang et al.* [2012]. All synthetic products were washed repeatedly with deionized water to remove other ions and were then dried at 60 °C.

The Al concentration incorporated in each solid phase (Table 1) was determined by atomic absorption spectroscopy (AAS) of samples dissolved in concentrated HCl. To confirm the purity of the synthetic samples, powder XRD was performed. XRD patterns for the HGL* series were reported by *Jiang et al.* [2012], while the remaining series were measured with a D/MAX-2400 XRD instrument at the Institute of Geology and Geophysics, Chinese Academy of Sciences (IGGCAS), with monochromatized CuKα radiation operating at 40 kV and 40 mA. Structural refinement and unit cell parameters were calculated for all XRD traces using JADE software, results of which are shown in Table 2.

Transmission electron microscope (TEM) images of the HFh* and HGL* series were reported by *Jiang et al.* [2012] and those for the GT* series were obtained using a Hitachi H800 microscope with an accelerating voltage of 175 kV at the University of Science and Technology, Beijing. For goethite samples GT0 and GT8, the length and thickness of more than 100 particles were measured. The grain size distribution of both samples has a lognormal distribution; mean particle sizes for samples GT0 and GT8 are listed in Table 2.

DRS measurements were made at wavelengths from 300 to 800 nm in 0.5 nm steps at a scan speed rate of 300 nm/min using a Varian Cary 5000 spectrophotometer equipped with a $BaSO_4$-coated integrating sphere. The DRS data were smoothed using the Varian instrument software (Savitzky-Golay method) with a filtering factor of 5, and were then transformed into Kubelka-Munk (K-M) functions $[(1-R)^2/2R]$, where R is the reflectance. The second-derivatives of the K-M functions were calculated using the Varian software with a filtering factor of 29. The characteristic band positions of hematite and goethite are ~535 nm ($P_{535\ nm}$) and ~425 nm ($P_{425\ nm}$), ~480 nm ($P_{480\ nm}$), respectively [*Torrent et al.*, 2007; *Jiang*

et al., 2014a]. The exact position of these characteristic bands may shift due to Al substitution. In this paper, we use $P_{535\ nm}$ and $P_{425\ nm}$, $P_{480\ nm}$ to represent the characteristic bands of hematite and goethite. The amplitudes of the hematite ($I_{535\ nm}$) and goethite ($I_{425\ nm}$, $I_{480\ nm}$) bands, measured as the difference between the band second-derivative minimum and the adjacent longer wavelength maximum (see *Jiang et al.* [2014] and *Liu et al.* [2011] for a detailed illustration of these measurements) are proportional to the concentration of hematite and goethite, respectively, and can thus be used as proxies for relative changes in mass concentration of goethite and hematite [*Liu et al.*, 2011; *Scheinost et al.*, 1998; *Sellitto et al.*, 2009; *Torrent et al.*, 2007].

For each synthetic sample, 10 subsamples were prepared based on a mixture of blank background material (described below) with different concentrations of pure hematite and goethite. For example, a series of samples was created by adding 1 mg, 2 mg, 3 mg, …, 10 mg of hematite sample HFh0 to background powder, mixing gently, and creating a 500 mg subsample. In this manner, 10 subsamples of sample HFh0 were produced with hematite concentrations of 2%, 4%, 6%, …, 20%, respectively. Other subsamples were prepared following the same method to produce 100 subsamples from combinations of hematite or goethite and background powder. DRS measurements were repeated 3 times and the average spectrum was calculated. To simulate natural conditions, the background powder was prepared using a geological material rather than a standard white reference (such as $BaSO_4$, CaF_2 or quartz powder). A sample of weakly weathered loess collected from the last glacial stratum on the Chinese Loess Plateau (L1 from the Luochuan section) was ground and treated with a CBD solution (buffered at pH ~7) to remove any hematite and goethite. The method is adopted from *Mehra and Jackson* [1960]. 1.2 g per 50 mL of dithionite was added and the suspension was stirred at 60 °C for half an hour before being placed in a reciprocating shaker at 25 °C for 16 hours. The residue was washed three times with deionized water and dried at

35 °C. This dissolution process was repeated 3 times and the residue was retained as the background powder. The post-CBD background powder was not perfectly 'clean' (Figure S1). Although almost no hematite was detected, a significant amount of goethite remained. Therefore, the goethite band intensity was determined for the background powder and its contribution was subtracted from DRS characterization of the prepared mixtures.

The isothermal remanent magnetization (IRM) was acquired in a forward field of 1 T or 2 T, after which reverse fields of -100 mT and -300 mT were applied. The corresponding forward and backfield IRMs are referred to as $IRM_{1\,T}$, $IRM_{2\,T}$, $IRM_{-100\,mT}$, and $IRM_{-300\,mT}$, respectively. HIRM is the most widely used proxy for high coercivity minerals, such as hematite and goethite [*Liu et al.*, 2007; *Thompson and Oldfield*, 1986], and is traditionally calculated as $HIRM = (IRM_{1\,T} + IRM_{-300\,mT})/2$ [*Bloemendal et al.*, 1992]. Theoretically, HIRM is the remanent magnetization acquired by particles with coercivities of remanence larger than the reverse field (RF) but smaller than the forward field (FF). Thus, a more general definition is $HIRM_{(FF,\,RF)} = (IRM_{FF} + IRM_{RF})/2$. Correspondingly, $HIRM_{(FF1,\,RF1)} - HIRM_{(FF1,\,RF2)} = HIRM_{(-RF2,\,RF1)}$ when RF1 > RF2, which is the difference between two HIRMs measured with the same FF but with different RFs and represents the remanence acquired by particles with coercivities of remanence bounded by the two RFs. Similarly, $HIRM_{(FF1,\,RF1)} - HIRM_{(FF2,\,RF1)} = HIRM_{(FF1,\,-FF2)}$ when FF1 > FF2. This definition gives HIRM wider applicability when particles have a more complex coercivity distribution (Figure 1).

For simplicity, HIRMs measured with different FFs and RFs are generally referred to as HIRMs. All remanences were measured with a Princeton Measurements Corporation vibrating sample magnetometer (Micromag VSM 3900). In order to determine the blocking temperature of goethite (T_b) in natural samples, which is the temperature at which the goethite changes from the stable single domain (SD) to the superparamagnetic (SP) state,

temperature-dependent HIRM curves were measured. Hematite in natural samples is almost saturated at 2.5 T, so $HIRM_{(5\ T,\ -2.5\ T)}$ was measured from 150 to 400 K using a Quantum Design Magnetic Property Measurements System (MPMS) at IGGCAS [*Jiang et al.*, 2014] to eliminate the influence of both hematite and magnetite. First, samples were cooled from room temperature to 150 K in zero field, and then an IRM was imparted in a 5 T field. Then, the IRM was measured in zero field from 150 K to 400 K (this warming curve is referred to as $IRM_{5\ T}$). Samples were then cooled again to 150 K in zero field, and an IRM was imparted in a 2.5 T RF and was thermally demagnetized from 150 K to 400 K. The corresponding curve is referred to as $IRM_{-2.5\ T.}$ The temperature dependence of $HIRM_{(5\ T,\ -2.5\ T)}$ is calculated by $[IRM_{5\ T} + IRM_{-2.5\ T}]/2$. To determine the T_b of synthetic goethite samples, thermal remanent magnetization (TRM) was acquired by cooling from 400 K in a field of 2.5 T. Then, remanent magnetization curves were measured from 20 K to 350 K in zero field.

3. Results

3.1. XRD, SEM, and TEM results

The grain size of the prepared hematites spans from 20 to ~400 nm (Figure 2a-e). The hematite particles are platy in the HFh* series and are granular in the HGL* series. XRD spectra confirm that only hematite is present in the HFh* and HGL* series (Figure 3). For the HFh* hematites, particle diameter increases with increasing Al content up to 6.8% (Table 2; to 12.9% according to more samples in *Jiang et al.* [2012]). In contrast, HGL* hematites have Al content up to 26.6% and much finer and more poorly crystallized particles (Table 1 and 2, Figure 3d, e). However, for hematite, the maximum limit for Al substitution is ~16% [*Cornell and Schwertmann*, 2003]. The Al substitution level in HGL* samples is likely overestimated because of Al-oxyhydroxide and probably corundum, which can be produced in hematite by heating Al-goethite at 800 °C [*Wells*, 1989]. However, no corundum or

Al-oxyhydroxide peaks were found in XRD results for any hematite samples, so that if they are present, their concentration must be under the detection limit of XRD analysis (5%). Excess Al may have developed in local concentrations as an amorphous, Al-rich exsolution rim or rind on the surface of individual hematite crystals or at boundaries between domains [*Watari et al.*, 1983], which is not detectable by XRD [*Wells, 1989*]. Therefore, HGL30, irrespective of the initial Al proportion in the synthesis, probably has no more than 16% Al in the final hematite produced. That is why HGL20 and HGL30 have similar crystal characteristics (Figure 3d, e) and DRS band positions (Figure 4a).

The characteristic lattice planes of goethite in the measured XRD spectra confirm the purity of the GT* series (Figure 3). The goethite crystallinity decreases with increasing Al content (Figure 3), a property that is confirmed by TEM images (Figure 2f-j). The goethite sample with no Al substitution (GT0, Figure 2f) has needle-like particles. With increasing Al content the particles become smaller and rounder, as was also found by *Jiang et al.* [2014a]. For samples GT16, GT20, and GT30, crystallinity is too poor to identify single goethite particles.

3.2. DRS results

3.2.1. Single mineral

The characteristic hematite and goethite band positions are independent of mineral concentration (Figure 4a, b, c), which indicates that the DRS band position is an intrinsic property of hematite and goethite. However, $P_{535\,nm}$, $P_{425\,nm}$, and $P_{480\,nm}$ changes with different degrees of Al substitution (Figure 4d, e, f). For the hematite series, $P_{535\,nm}$ shifts to shorter wavelengths with increasing Al substitution (Figure 4d), which is consistent with previous studies [*da Costa et al.*, 2002; *Kosmas et al.*, 1986; *Liu et al.*, 2011; *Torrent and Barrón*, 2003]. The $P_{480\,nm}$ bands for Al-goethite also trend toward shortened wavelengths with increasing Al content (Figure 4c), but $P_{425\,nm}$ does not have a significant trend with Al

substitution (Figure 4b).

In hematite and goethite, $P_{535\ nm}$ and $P_{480\ nm}$ are assigned to the $2(^6A_1) \rightarrow (^4T_1;(^4G))$ double exciton process [*Sherman and Waite*, 1985]. When Al is incorporated into the structure of hematite and goethite, bonding of smaller Al $(O, OH)_6$ octahedra with larger $Fe(O, OH)_6$ octahedra gives rise to distortions that alter the Fe to (O, OH) distances and lowers the crystal symmetry, which alters the ligand field and shifts the band positions to lower wavelengths [*Burns*, 1993; *Scheinost et al.*, 1999]. However, *Scheinost et al*. [1999] also calculated the energy of the $^6A_1 \rightarrow (^4E;^4A_1)$ transition ($P_{425\ nm}$) and found that it is independent of the crystal field splitting energy, which means that $P_{425\ nm}$ should be constant. This explains why $P_{425\ nm}$ has the weakest relationship with Al content. However, *Jiang et al.* [2014a] argued that $P_{425\ nm}$ is dependent on Al substitution and that the mechanism is also consistent with variation of $P_{480\ nm}$ with Al content. Therefore, more work needs to be done to confirm the influence of Al on $P_{425\ nm}$, but $P_{480\ nm}$ is much more sensitive to Al content in goethite.

For mineral mixtures of hematite or goethite, the DRS second derivative curves are shown in Figure S2. Both hematite ($I_{535\ nm}$) and goethite ($I_{425\ nm}$, $I_{480\ nm}$) DRS intensities are linearly correlated to mass percentage (Figure 5), which confirms the feasibility of DRS band intensity to estimate the mass concentration of hematite and goethite. For samples with different synthetic hematite or goethite contents, $I_{425\ nm}$, $I_{480\ nm}$, and $I_{535\ nm}$ are, however, influenced by Al substitution (Figure 5). Al incorporation changes Fe-to-Fe distances and, thus, influences the magnetic coupling of electron spins at neighboring Fe centers and may modify band intensity [*Kosmas et al.*, 1986; *Jiang et al.*, 2014a]. $I_{535\ nm}$ is suppressed for samples with higher Al content, such as HGL20 and HGL30 (Figure 5a). When Al content is less than ~8% (HFh0, HFh4, and HFh8), $I_{535\ nm}$ has a consistent linear relationship with the hematite mass percentage (Figure 5a). Similar behavior is observed in the goethite series,

when Al substitution exceeds ~15% (such as GT20 and GT30), where $I_{425\ nm}$ and $I_{480\ nm}$ lose sensitivity to goethite concentration.

3.2.2. Hematite and goethite mixtures

Hematite and goethite will usually co-exist in natural soils and sediments. To test the reliability of $I_{425\ nm}$, $I_{480\ nm}$, and $I_{535\ nm}$ to quantify goethite and hematite in such materials, we measured DRS curves for mixtures of synthetic hematite and goethite. In Figure 5a, two groups of hematite can be identified. Hematites with lower Al contents, such as HFh0, HFh4, and HFh8, have a consistent linear relationship between $I_{535\ nm}$ and concentration. Hematites with higher Al contents, such as HGL20 and HGL30, have reduced $I_{535\ nm}$ values. For goethite, high Al substitution also suppresses $I_{425\ nm}$ and $I_{480\ nm}$ (Figure 5b, c).

We prepared 4 groups of mixed samples, HFh0+GT0, HFh8+GT8, HFh0+GT30, and HGL30+GT30, which correspond to mixtures of pure hematite and goethite, and a range of hematite and goethite samples with variable Al contents. In each group, 10 sub-samples were prepared with hematite/goethite ratios ranging from 0.125 to 10. The second-derivative curves of all mixed samples are shown in Figure S3.

The DRS intensity ratio $I_{535\ nm}/(I_{535\ nm} + I_{425\ nm})$ has been related to the hematite/(hematite + goethite) ratio (denoted as H/(H + G)) using a best-fit second-order polynomial, which is consistent with the study of *Torrent et al.* [2007]. However, the calibration curve of *Torrent et al*. [2007]: $Y=-0.133+2.871\times X-1.709\times X^2$, where Y represents H/(H+G) and X represents $I_{535\ nm}/(I_{535\ nm} + I_{425\ nm})$, does not produce the best fitting results, especially for mixtures that contain large Al contents in hematite or goethite (blue dashed lines, Figure 6a-d). Instead, the best estimated relationship changes between the 4 sets of mixtures (black lines, Figure 6a-d) and demonstrates the effects of Al substitution. Alternative proxies for goethite/hematite (G/H) are given by the ratios $I_{425\ nm}/I_{535\ nm}$ and $I_{480\ nm}/I_{535\ nm}$. When Al substitution is < ~8 mol % in

the hematite and goethite components, the G/H and $I_{425\ nm}/I_{535\ nm}$ or $I_{480\ nm}/I_{535\ nm}$ ratios correlate linearly (Figure 6e-h, i-k). When considered in combination, the two groups with Al substitution < ~8 mol % can be fitted with a single line (Figure 7); $G/H = 1.56 \times (I_{425\ nm}/I_{535\ nm}) + 0.07$; or $G/H = 6.32 \times (I_{480\ nm}/I_{535\ nm}) + 0.19$. The 95% confidence intervals on the slope and intercept values are {1.56 ± 0.12, 0.07 ± 0.32} and {6.32 ± 0.34, 0.19 ± 0.23} for the two equations, respectively. The intercept term is statistically indistinguishable from zero, therefore, we define $G/H = 1.56 \times (I_{425\ nm}/I_{535\ nm})$ or $G/H = 6.32 \times (I_{480\ nm}/I_{535\ nm})$ as suitable transfer functions to estimate the relative abundances of hematite and goethite, when Al substitution is less than ~8%.

The sample set consisting of pure hematite and highly Al-substituted goethite has a much lower gradient than the other sample sets (Figure 6g, k). This is consistent with the lower sensitivity of $I_{425\ nm}$ and $I_{480\ nm}$ when Al substitution is high (Figure 5). Similarly, the gradient will be greater if highly Al-substituted hematite is mixed with Al-poor goethite. When Al substitution is high in both hematite and goethite, a significant intercept occurs on the $I_{425\ nm}/I_{535\ nm}$ axis and $I_{480\ nm}/I_{535\ nm}$ axis. This intercept results from an additional contribution to $I_{425\ nm}$ and $I_{480\ nm}$ because the signature of highly substituted hematite is partially superimposed onto the goethite band (Figure S3). The second derivative 425 nm goethite band results from the electron transition: $A_1{}^6 \rightarrow A_1{}^4;E^4$ [*Scheinost et al.*, 1998]. This transition may, however, overlap with band ranges for other iron oxides, such as hematite [*Cornell and Schwertmann*, 2003]. For hematite this electron transition will usually produce a crystal field band at wavelengths slightly longer than 425 nm. The presence of Al in hematite will, however, offset the band position to shorter wavelengths that overlap with those of goethite [*Kosmas et al.*, 1986; *Liu et al.*, 2011]. A similar mechanism may apply to additional contributions to $I_{480\ nm}$, which represents the intensity of the $2(^6A_1) \rightarrow (^4T_1;(^4G))$ double exciton process.

3.3. Magnetic results

Generally, $HIRM_{(1\ T,\ -300\ mT)}$ and $HIRM_{(2\ T,\ -300\ mT)}$ both increase linearly with hematite and goethite concentration (Figure 8a-d). However, different synthetic hematite and goethite sample series have different ascending slopes, which indicate different abilities to acquire HIRM. For example, HFh8 is more efficient in acquiring $HIRM_{(1\ T,\ -300\ mT)}$ and $HIRM_{(2\ T,\ -300\ mT)}$ than the other hematite samples (Figure 8a) and GT0 is the only analyzed goethite sample that efficiently acquires HIRM (Figure 8b). Such behavior indicates that HIRM values not only depend on the concentration of hematite and goethite, but that they also vary with Al substitution and grain size.

The influence of Al substitution on hematite HIRM is complicated. For SD particles, a positive correlation between hematite hardness and Al content is observed due to development of lattice defects that arise from Al incorporation or internal stress [*Jiang et al.*, 2012; *Stanjek and Schwertmann*, 1992; *Wells et al.*, 1999]. Defects resulting from Al incorporation inhibit magnetic domain rotation and flipping, which causes an increase in magnetic hardness. The coercivity of hematite also increases with grain size in the SD size range [*Jiang et al.*, 2012, 2014b; *Özdemir and Dunlop*, 2014]. *Özdemir and Dunlop* [2014] demonstrated that the traditional $HIRM_{(1\ T,\ -300\ mT)}$ parameter is only sensitive to hematite particles with sizes from ~0.3 to 3 μm, which is consistent with results for HFh8 (Figure 8a). The remanence of hematite also increases with grain size [*Dekkers and Linssen*, 1989; *Dunlop*, 1971; *Özdemir and Dunlop*, 2014]. However, beyond a certain Al substitution level (7% ~ 8%, according to *Jiang et al.* [2012]), hematite grain size decreases gradually to the SP region and hematite loses its ability to retain a magnetic remanence (e.g., HGL20 and HGL30). Therefore, HFh8, which has the largest grain size but a low Al content (< 8%), has the largest HIRM among all of the studied hematite samples.

Al-goethite has more complicated magnetic behavior than Al-hematite. Generally, with

increasing Al substitution, Al ions cluster preferentially along the same sub-lattice where earlier substitutions occurred [*Pollard et al.*, 1991] and the bulk magnetization increases due to unbalanced moments, as reported in previous studies [*Dekkers*, 1989]. However, further Al incorporation into the structure decreases the T_b of Al-goethite by increasing crystal defects and further diluting magnetic interactions of adjacent layers or by reducing grain size [*Jiang et al.*, 2014a; *Liu et al.*, 2004]. In TRM demagnetization curves for goethite (Figure S4), T_b values for GT8, GT16, GT20, and GT30 are 292 K, 252 K, 205 K, and 170 K, respectively, which are all below room temperature (~300 K). These results are consistent with those of *Jiang et al.* [2014a] where ~8% Al substitution is sufficient to decrease T_b to below room temperature and thus, GT8, GT16, GT20, and GT30 become SP and lose their ability to acquire HIRM at room temperature (Figure 8b, d).

The HIRM of hematite is almost 10 times larger than that of goethite (compare HFh8 and GT0) because the ferromagnetism of goethite is extremely weak but hard [*Dekkers*, 1989; *Liu et al.*, 2004]. Due to the low magnetization of goethite, large fields are needed to deflect magnetic moments. As a result, significant remanence acquisition of goethite generally begins at above 1 T and sometimes 20 T is insufficient to saturate goethite [*Dekkers*, 1989; *Rochette et al.*, 2005]. Moreover, natural goethite has small crystals and is often Al-substituted, which suppresses T_b to below room temperature and, thus, goethite becomes SP and loses its ability to acquire HIRM. Therefore, when dealing with natural samples that contain both hematite and goethite, HIRM is usually dominated by the hematite component.

Liu et al. [2007] proposed the 'L-ratio' parameter to evaluate the reliability of HIRM to quantify hematite concentration. The L-ratio is the ratio of $HIRM_{(1\ T,\ -300\ mT)}$ and $HIRM_{(1\ T,\ -100\ mT)}$, which provides a representation of the coercivity distribution of 'hard' magnetic minerals. In this study, to test the influence of Al substitution on the coercivity distribution of hematite and goethite, we introduce a biplot of $HIRM_{(1\ T,\ -300\ mT)}$ and $HIRM_{(1\ T,\ -100\ mT)}$. This is a revised

representation of the L-ratio based on $\Delta HIRM_{(1\ T,\ -300\ mT)}/\Delta HIRM_{(1\ T,\ -100\ mT)}$, where the gradient of this plot characterizes variation of relative remanence contributions of magnetic minerals with coercivities in the intervals [0.3, 1] T and [0.1, 1] T across a group of samples. For a mixture series produced with a single hematite, $\Delta HIRM_{(1\ T,\ -300\ mT)}/\Delta HIRM_{(1\ T,\ -100\ mT)}$ remains constant and individual mixtures plot along a straight line. In contrast, collections of mixing series produced with different synthetic hematites have distinguishable $\Delta HIRM_{(1\ T,\ -300\ mT)}/\Delta HIRM_{(1\ T,\ -100\ mT)}$ ratios and each series plots on a different line (Figure 8e). Generally, hematites with higher Al have higher $\Delta HIRM_{(1\ T,\ -300\ mT)}/\Delta HIRM_{(1\ T,\ -100\ mT)}$ ratios (Figure 8g). When Al content is relatively small (< ~8%), such as in samples HFh0, HFh4, and HFh8, hematite has stable SD behavior, as we discussed above, with increasing Al, the coercivity of SD hematite increases, which is reflected by an increasing $\Delta HIRM_{(1\ T,\ -300\ mT)}/\Delta HIRM_{(1\ T,\ -100\ mT)}$ ratio. Highly Al substituted hematite is usually transformed from a goethite precursor [*Cornell and Schwertmann*, 2003; *Jiang et al.*, 2012], such as HGL20 and HGL30, therefore, the coercivity of HGL20 is much higher than the HFh* hematites (Figure 10e in *Jiang et al.* [2012]). That is the reason why the $\Delta HIRM_{(1\ T,\ -300\ mT)}/\Delta HIRM_{(1\ T,\ -100\ mT)}$ ratio of HGL20 is nearly 1. However, HGL30 has the highest Al substitution and shows more SP behavior [*Jiang et al.*, 2012], so it loses its ability to retain a remanence, and $\Delta HIRM_{(1\ T,\ -300\ mT)}/\Delta HIRM_{(1\ T,\ -100\ mT)}$ becomes unreliable. For goethite, only samples with no Al substitution have a good linear relationship between $HIRM_{(1\ T,\ -300\ mT)}$ and $HIRM_{(1\ T,\ -100\ mT)}$ (Figure 8f); other samples produce unreliable $\Delta HIRM_{(1\ T,\ -300\ mT)}/\Delta HIRM_{(1\ T,\ -100\ mT)}$ values because they acquire minimal remanence (Figure 8b).

4. Discussion

The ubiquity of Al in weathering environments results in most Fe oxides in soils being

Al-substituted [*Cornell and Schwertmann*, 2003; *Fontes and Weed*, 1991; *Friedl and Schwertmann*, 1996; *Wiriyakitnateekul et al.*, 2007]. According to previous studies and results presented here, Al substitution affects both DRS and magnetic properties [*Dekkers*, 1989; *Dekkers and Linssen*, 1989; *Jiang et al.*, 2014; *Liu et al.*, 2011; *Malengreau et al*., 1997; *Torrent and Barrón*, 2003], such as HIRM.

Several conclusions are evident from our results. First, when Al substitution exceeds ~8%, $I_{425\ nm}$, $I_{480\ nm}$, and $I_{535\ nm}$ are suppressed significantly (Figure 5). Second, when Al substitution is high (>~8%) hematite grain size decreases gradually to SP sizes, so that HIRM is reduced significantly (Figure 8a, c). Third, HIRM of goethite is also reduced because more than 8% Al content decreases the T_b of goethite to below room temperature and, thus, goethite becomes SP at room temperature (Figure 8b, d; Figure 5 of *Jiang et al*. [2014a]). Therefore, it is not straightforward to use DRS or HIRM in isolation to (semi-)quantify hematite and goethite concentrations without proper evaluation of the extent of Al substitution. To estimate hematite and goethite concentrations accurately, it is essential to determine the Al-content *a priori* in either an absolute or relative manner. DRS and magnetic properties of hematite and goethite are influenced significantly by Al substitution, therefore, these properties can constrain the concentration of hematite and goethite in natural archives. Several studies have combined DRS and magnetic methods to constrain Al substitution in soils [*Jiang et al.*, 2014a; *Liu et al.*, 2004, 2015; *Malengreau et al.*, 1997]. Our more systematic data reveal that characteristic DRS band positions ($P_{535\ nm}$ and $P_{480\ nm}$) decrease with increasing Al substitution (Figure 4d, f) while $\Delta HIRM_{(1\ T,\ -300\ mT)}/\Delta HIRM_{(1\ T,\ -100\ mT)}$ correlates positively to Al substitution (Figure 8g). Therefore, we combine published results and our new data to better constrain the extent of Al substitution in Chinese loess and to test the feasibility of applying DRS band intensities to estimate relative hematite and goethite concentrations.

Two loess/paleosol sequences containing last glacial/interglacial and Holocene deposits

were selected from the Chinese Loess Plateau (Luochuan section, 35°43.604'N, 109°25.813'E, 1097 m elevation) and the eastern Tibetan Plateau (Ganzi section, 31°30.994'N, 99°58.590'E, 3455 m elevation). These locations have different pedogenic environments and sediment source areas [*Hu et al.,* 2015], which could result in diverse hematite and goethite properties. In Figure 9a, b, sediments from both sections have $P_{480\ nm}$ values that range between 482 and 487 nm, which corresponds to unsubstituted goethite in Figure 4f. However, the $P_{535\ nm}$ range for both sections (530 nm to 545 nm) is too large to estimate Al substitution based on Figure 4d. More data are needed in future to better estimate Al substitution based on $P_{535\ nm}$. For both sections, $HIRM_{(1\ T,\ -300\ mT)}$ and $HIRM_{(1\ T,\ -100\ mT)}$ correlate linearly, which indicates that the $\Delta HIRM_{(1\ T,\ -300\ mT)}/\Delta HIRM_{(1\ T,\ -100\ mT)}$ ratio is relatively stable and, thus, that Al substitution remains consistent throughout the two sections, which enables the use of HIRMs as a proxy for hematite concentration. For the Luochuan and Ganzi loess (excluding the marine isotope stage (MIS) 3 warm period), $\Delta HIRM_{(1\ T,\ -300\ mT)}/\Delta HIRM_{(1\ T,\ -100\ mT)}$ is 0.17 and 0.31, respectively (Figure 9c), which is indicative of hematite with Al substitution < ~8% (Figure 8e, g).

Al substitution of goethite can also be constrained through its T_b or Néel temperature (T_N) [*Jiang et al.,* 2014a; *Liu et al.,* 2004] because Al substitution decreases T_b and T_N though a dilution process of magnetic interaction both by Al content and crystal defects [*Liu et al.,* 2004]. T_N is determined using temperature dependence of susceptibility or in-field magnetization curves, which, however, is dominated by ferrimagnetic minerals in natural samples. Therefore, *Jiang et al.* [2014a] developed a method using HIRM-T curves to determine the T_b of goethite. By comparing results from synthetic Al-goethite, they further constrained Al substitution of goethite in the Luochuan loess to be < 8%. By applying the same techniques, goethite T_b in the Ganzi loess is found to be 300 ~ 325 K (Figure 9d), which is consistent with that of the Luochuan loess [*Jiang et al.,* 2014], which is also indicative of

Al substitution < ~8%. For Chinese loess, this estimate is reasonable. Synthesis experiments suggest that the maximum feasible substitution in terms of Al/(Al + Fe) is 33% in goethite and 16% in hematite [*Cornell and Schwertmann*, 2003]. High Al substitution of up to 32% has been observed in goethite from tropical and subtropical soils, bauxites, and saprolites. In these highly weathered soils, Al-goethite forms in contact with Al sources such as feldspars, micas, and kaolinite, which may explain their high Al substitution [*Cornell and Schwertmann*, 2003, and references therein]. However, Chinese loess forms in a temperate semi-arid region and is not usually highly weathered. For such cases, where Al substitution of hematite and goethite is <8%, the relative concentration of these two components can be estimated using the proposed relationship: goethite/hematite = $1.56 \times (I_{425\ nm}/I_{535\ nm})$ or goethite/hematite = $6.32\times (I_{480\ nm}/I_{535\ nm})$ (Figure 7).

HIRM can also provide a semi-quantitative estimate of hematite concentration (Figure 8a, c). However, HIRM is sensitive to the underlying hematite coercivity distribution. The traditional $HIRM_{(1\ T,\ -300\ mT)}$ parameter is dominated by hematite particles in the 0.3-3 μm size range [*Özdemir and Dunlop*, 2014], rather than by the nm-scale pedogenic hematite that is widely present in soils and sediments [*Chen et al.*, 2010; *Hu et al.*, 2013]. Therefore, in natural hematites with different origins, HIRM should be tuned to specific hematite coercivity distributions in order to robustly estimate true concentration variations. On the basis of IRM decomposition [*Heslop et al.*, 2002; *Kruiver et al.*, 2001], *Hu et al.* [2013] suggested that the mean remanent coercivity of pedogenic hematite in Chinese loess is 126 mT with a standard deviation in $\log_{10}$-space of 0.2. Thus, 95% of pedogenic hematite is expected to have remanent coercivity in the range 50-317 mT. In contrast, the remanent coercivity of lithogenic hematite is higher with a greater dispersion (~340 mT to ~5 T). Therefore, the traditional $HIRM_{(1\ T,\ -300\ mT)}$ parameter is better suited to representing lithogenic hematite variations. For pedogenic hematite, however, $HIRM_{(1\ T,-100\ mT)} - HIRM_{(1\ T,-300\ mT)}$ is more appropriate because

it provides a representation of particles with remanent coercivities between 100 and 300 mT, which should not include a significant contribution from ferrimagnetic minerals [*Deng et al.*, 2006; *Hu et al.*, 2013; *Liu et al.*, 2005]. Therefore, $HIRM_{(FF, RF)}$ is a more useful parameter than the traditional $HIRM_{(1\ T, -300\ mT)}$.

In certain cases, particularly when considering long-term climate variability, relative hematite and goethite concentration variations are sufficient for environmental reconstruction. This approach requires the properties of hematite and goethite (i.e., degree of Al substitution and grain size) to be effectively invariant through time. If this is the case, a linear trend should be observed between $HIRM_{(1\ T, -300\ mT)}$ and $HIRM_{(1\ T, -100\ mT)}$. For example, $HIRM_{(1\ T, -300\ mT)}$ versus $HIRM_{(1\ T, -100\ mT)}$ follows a linear relationship through the Luochuan section (Figure 9b), which indicates that hematite properties are relatively stable throughout the studied sequence. In contrast, Ganzi subpaleosol samples from the MIS 3 warm period are characterized by $\Delta HIRM_{(1\ T, -300\ mT)}/\Delta HIRM_{(1\ T, -100\ mT)} \approx 0.55$ (Figure 9c), which is significantly higher than for other samples and indicates higher Al substitution (>~8% from Figure 8e, g). Previous environmental magnetic and geochemical analyses also suggest enhanced chemical weathering in the Ganzi loess, particularly during early MIS 3 [*Hu et al.*, 2015], which supports our Al estimation from $\Delta HIRM_{(1\ T, -300\ mT)}/\Delta HIRM_{(1\ T, -100\ mT)}$. Based on DRS alone, enhanced Al substitution in hematite would imply that the absolute hematite concentration would be underestimated in the MIS 3 part of the Ganzi section (Figure 5a). We do not, however, observe a significant change of $P_{535\ nm}$ in Ganzi loess because $P_{535\ nm}$ is more effective at separating micron-scale hematite from nm-scale hematite rather than differentiating between nm-scale hematite [unpublished results]. It is, therefore, important to combine magnetic and DRS properties to estimate Al contents and grain size variations in hematite and goethite. This is more crucial in long sequences, such as deep-sea sediments or long eolian records, where stronger environmental variability may have occurred over

extended time periods or where provenance variations are more important and estimates of hematite/goethite concentration may be biased strongly.

5. Limitations and future studies

The above results are based on limited synthetic hematite and goethite samples with nm sizes. In natural samples, both micro- and nano-sized hematite and goethite exist. Natural goethite in rocks is usually well-crystalized and micro-sized [*Chaparro et al.*, 2006; *Dekkers*, 1989; *Gehring and Heller*, 1991], while in soils it is poorly crystalized and nano-sized [*Cornell and Schwertmann*, 2003; *Maher et al.*, 2004]. Therefore, our results are more suitable for applying to soils rather than rocks. Moreover, hematite and goethite synthesized in different ways may have variable magnetic properties [*Jiang et al.*, 2012, 2014a]. Therefore, ~8% is estimated as a separation point for low and high Al substitution based on our samples rather than representing an absolute boundary for DRS or magnetic properties of hematite and goethite. For more robust estimation of Al substitution and to address questions of provenance and source changes in natural archives, further, more detailed, DRS and magnetic study of a wider grain size range of hematite and goethite is needed. It is also important to evaluate the influence of synthesis methods on the DRS and magnetic properties of hematite and goethite. Nevertheless, our study confirms that Al substitution must be considered when estimating hematite and goethite concentrations using DRS or magnetic methods. The proposed combined approach will help to develop a clearer picture of Al substitution and its variation in natural hematite and goethite, and in using DRS and magnetic data more reliably. For instance, the $\Delta HIRM_{(1\ T,\ -300\ mT)}/\Delta HIRM_{(1\ T,\ -100\ mT)}$ ratio and HIRM-T curves are useful for checking whether Al substitution in hematite and goethite is relatively stable through a sediment sequence, which will enable use of DRS band intensity and HIRM to represent hematite and goethite concentration trends.

6. Conclusions

We assessed the feasibility of using DRS and magnetic methods to estimate hematite and goethite concentrations using synthetic hematite and goethite and tested our approach on Chinese loess/paleosol sequences. DRS band positions and intensities are influenced by both Al substitution and particle size, two properties that often covary. However, for nm-scale hematite and goethite with low to medium (< ~8%) Al substitution, new transfer functions are established here that relate the DRS band intensity ratio to relative concentration: goethite/hematite = 1.56 × ($I_{425\ nm}/I_{535\ nm}$) and goethite/hematite = 6.32 × ($I_{480\ nm}/I_{535\ nm}$). The new functions can be applied reliably to Chinese loess and paleosol sequences where Al substitution is < ~8% and relatively constant. However, for long sediment sequences, it is necessary to estimate Al substitution using both DRS and magnetic methods before performing goethite and hematite quantification. Both Al substitution and grain size control the magnetic properties of hematite, so $HIRM_{(FF,\ RF)}$ is proposed to indicate variations in hematite with different origins.

Acknowledgements

This study was supported by the National Natural Science Foundation of China (No. 41374073 and 41430962), the National Program on Global Changes and Air-Sea Interaction (No. GASI-04-01-02), and the Chinese Continental Shelf Deep Drilling Program (GZH201100202). Pengxiang Hu was further supported by the China Scholarship Council ([2013]3009). David Heslop and Andrew Roberts were supported by Australian Research Council Discovery Project DP110105419. We thank Dr. Chunxia Zhang for assistance with XRD measurements, Dr. Xiang Zhao for helpful discussions, and Dr. Chuan Lu for technical support. All results shown in the figures and tables in this paper are available from the PANGAEA database.

References

Ao, H., M. J. Dekkers, L. Qin, and G. Xiao (2011), An updated astronomical timescale for the Plio-Pleistocene deposits from South China Sea and new insights into Asian monsoon evolution, *Quat. Sci. Rev.*, *30*, 1560-1575.

Balsam, W., J. F. Ji, and J. Chen (2004), Climatic interpretation of the Luochuan and Lingtai loess sections, China, based on changing iron oxide mineralogy and magnetic susceptibility, *Earth Planet. Sci. Lett.*, *223*, 335-348.

Balsam, W., B. Ellwood, and J. F. Ji (2005), Direct correlation of the marine oxygen isotope record with the Chinese Loess Plateau iron oxide and magnetic susceptibility records, *Palaeogeogr. Palaeoclimatol. Palaeoecol.*, *221*, 141-152.

Balsam, W., J. F. Ji, D. Renock, B. C. Deaton, and E. Williams (2014). Determining hematite content from NUV/Vis/NIR spectra: Limits of detection, *Am. Mineral*., *99*, 2280-2291.

Barrón, V., and L. Montealegre (1986), Iron oxides and color of Triassic sediments - Application of the Kubelka-Munk theory, *Am. J. Sci.*, *286*, 792-802.

Barrón, V., and J. Torrent (1986), Use of the Kubelka-Munk theory to study the influence of iron-oxides on soil color, *J. Soil. Sci.*, *37*, 499-510.

Barrón, V., J. Torrent, and E. de Grave (2003), Hydromaghemite, an intermediate in the hydrothermal transformation of 2-line ferrihydrite into hematite, *Am. Mineral.*, *88*, 1679-1688.

Bloemendal, J., J. W. King, F. R. Hall, and S. J. Doh (1992), Rock magnetism of late Neogene and Pleistocene deep-sea sediments: Relationship to sediment source, diagenetic processes, and sediment lithology, *J. Geophys. Res.*, *97*, 4361-4375.

Burns, R. G. (1993), Mineralogical applications of crystal field theory, In: Putnis, A., and R. C. Lieberman (Eds.), Cambridge Topics in Mineral Physics and Chemistry (5th Ed.), Cambridge University Press.

Chaparro, M. A. E., A. M. Sinito, J. C. Bidegain, and R. E. de Barrio (2006), Magnetic studies of natural goethite samples from Tharsis, Huelva, Spain, *Geofís. Int.*, *45*, 219-230.

Chen, T. H., Q. Q. Xie, H. F. Xu, J. Chen, J. F. Ji, H. Y. Lu, and W. Balsam (2010), Characteristics and formation mechanism of pedogenic hematite in Quaternary Chinese loess and paleosols, *Catena*, *81*, 217-225.

Cornell, R. M., and U. Schwertmann (2003), *The Iron Oxides: Structure, Properties, Reactions, Occurrences and Uses*, Wiley, Weinheim, Germany.

da Costa, G. M., E. Van San, E. De Grave, R. E. Vandenberghe, V. Barrón, and L. Datas (2002), Al hematites prepared by homogeneous precipitation of oxinates: Material characterization and determination of the Morin transition, *Phys. Chem. Miner.*, *29*, 122-131.

Deaton, B. C., and W. L. Balsam (1991), Visible spectroscopy: A rapid method for determining hematite and goethite concentration in geological materials, *J. Sediment. Res.*, *61*, 628-632.

Dekkers, M. J. (1989), Magnetic properties of natural goethite-I. Grain-size dependence of some low- and high-field related rockmagnetic parameters measured at room temperature, *Geophys. J. Int.*, *97*, 323-340.

Dekkers, M. J., and J. H. Linssen (1989), Rockmagnetic properties of fine-grained natural low-temperature hematite with reference to remanence acquisition mechanisms in red beds, *Geophys. J. Int.*, *99*, 1-18.

Deng, C. L., J. Shaw, Q. S. Liu, Y. X. Pan, and R. X. Zhu (2006), Mineral magnetic variation of the Jingbian loess/paleosol sequence in the northern Loess Plateau of China: Implications for Quaternary development of Asian aridification and cooling, *Earth Planet. Sci. Lett.*, *241*, 248-259

Dunlop, D. J. (1971), Magnetic properties of fine-particle hematite, *Ann. Geophys.*, *27*, 269-293.

Eyre, J. K., and D. P. E. Dickson (1995), Mössbauer spectroscopy analysis of iron-containing minerals in the Chinese loess, *J. Geophys. Res.*, *100*, 17925-17930.

Felix-Henningsen, P. (2000), Paleosols on Pleistocene dunes as indicators of paleo-monsoon events in the Sahara of East Niger, *Catena*, *41*, 43-60.

Fontes, M. P. F., and S. B. Weed (1991), Iron oxides in selected Brazilian oxisols: I. Mineralogy, *Soil Sci. Soc. Am. J.*, *55*, 1143-1149.

Friedl, J., and U. Schwertmann (1996), Aluminium influence on iron oxides. 18. The effect of Al substitution and crystal size magnetic hyperfine fields of natural goethites, *Clay Miner.*, *31*, 455-464.

Frost, B. R. (1991), Stability of oxide minerals in metamorphic rocks, *Rev. Mineral. Geochem.*, *25*, 467-487.

Hao, Q., F. Oldfield, J. Bloemendal, J. Torrent, and Z. Guo (2009), The record of changing hematite and goethite accumulation over the past 22 Myr on the Chinese Loess Plateau from magnetic measurements and diffuse reflectance spectroscopy, *J. Geophys. Res.*, *114*, B12101, doi:10.1029/2009JB006604.

Heslop, D., M. J. Dekkers, P. P. Kruiver, and I. H. M. van Oorschot (2002), Analysis of isothermal remanent magnetization acquisition curves using the expectation-maximization algorithm, *Geophys. J. Int.*, *148*, 58-64.

Hochella, M. F., S. K. Lower, P. A. Maurice, R. L. Penn, N. Sahai, D. L. Sparks, and B. S. Twining (2008), Nanominerals, mineral nanoparticles, and Earth systems, *Science*, *319*, 1631-1635.

Hu, P. X., Q. S. Liu, J. Torrent, V. Barrón, and C. S. Jin (2013), Characterizing and quantifying iron oxides in Chinese loess/paleosols: Implications for pedogenesis, *Earth Planet. Sci. Lett.*, *369–370*, 271-283.

Hu, P. X., Q. S. Liu, D. Heslop, A. P. Roberts, and C. S. Jin (2015), Soil moisture balance and magnetic enhancement in loess–paleosol sequences from the Tibetan Plateau and Chinese Loess Plateau, *Earth Planet. Sci. Lett.*, *369-409*, 120-132.

Ji, J. F., W. Balsam, and J. Chen (2001), Mineralogic and climatic interpretations of the Luochuan loess section (China) based on diffuse reflectance spectrophotometry, *Quat. Res.*, *56*, 23-30.

Ji, J. F., W. Balsam, J. Chen, and L. W. Liu (2002), Rapid and quantitative measurement of hematite and goethite in the Chinese loess-paleosol sequence by diffuse reflectance spectroscopy, *Clays Clay Mineral.*, *50*, 208-216.

Ji, J. F., J. Chen, W. Balsam, H. Lu, Y. Sun, and H. Xu (2004), High resolution hematite/goethite records from Chinese loess sequences for the last glacial-interglacial cycle: Rapid climatic response of the East Asian Monsoon to the tropical Pacific, *Geophys. Res. Lett.*, *31*, L03207, doi:10.1029/2003GL018975.

Jiang, Z. X., Q. S. Liu, V. Barrón, J. Torrent, and Y. J. Yu (2012), Magnetic discrimination between Al-substituted hematites synthesized by hydrothermal and thermal dehydration methods and its geological significance, *J. Geophys. Res.*, *117*, B02102, doi:10.1029/2011JB008605.

Jiang, Z. X., Q. S. Liu, C. Colombo, V. Barrón, J. Torrent, and P. X. Hu (2014a), Quantification of Al-goethite from diffuse reflectance spectroscopy and magnetic methods, *Geophys. J. Int.*, *196*, 131-144.

Jiang, Z. X., Q. S. Liu, M. J. Dekkers, C. Colombo, Y. J. Yu, V. Barrón, and J. Torrent (2014b), Ferro and antiferromagnetism of ultrafine-grained hematite, *Geochem. Geophys. Geosyst.*, *15*, 2699-2712.

Jordanova, N., D. Jordanova, Q. S. Liu, P. X. Hu, P. Petrov, and E. Petrovsky (2013), Soil formation and mineralogy of a rhodic luvisol - insights from magnetic and geochemical studies, *Global Planet. Change*, *110*, 397-413.

Kämpf, N., and U. Schwertmann (1983), Goethite and hematite in a climosequence in southern Brazil and their application in classification of kaolinitic soils, *Geoderma*, *29*, 27-39.

Kosmas, C. S., D. P. Franzmeier, and D. G. Schulze (1986), Relationship among derivative spectroscopy, color, crystallite dimensions, and A1 substitution of synthetic goethites and hematites, *Clays Clay Mineral.*, *34*, 625-634.

Kruiver, P. P., M. J. Dekkers, and D. Heslop (2001), Quantification of magnetic coercivity components by the analysis of acquisition curves of isothermal remanent magnetization, *Earth Planet. Sci. Lett.*, *189*, 269-276.

Liu, Q., J. Torrent, Y. Yu, and C. Deng (2004). Mechanism of the parasitic remanence of aluminous goethite [α-(Fe, Al)OOH], *J. Geophys Res.*, *109*, B12106, doi:10.1029/2004JB003352.

Liu, Q. S., S. K. Banerjee, M. J. Jackson, C. L. Deng, Y. X. Pan, and R. X. Zhu (2005), Inter-profile correlation of the Chinese loess-paleosol sequences during marine oxygen isotope stage 5 and indications of pedogenesis, *Quat. Sci. Rev.*, *24*, 195-210.

Liu, Q. S., A. P. Roberts, J. Torrent, C. S. Horng, and J. C. Larrasoaña (2007), What do the HIRM and S-ratio really measure in environmental magnetism? *Geochem. Geophys. Geosyst.*, *8*, Q09011, doi:10.1029/2007GC001717.

Liu, Q. S., J. Torrent, V. Barrón, Z. Q. Duan, and J. Bloemendal (2011), Quantification of hematite from the visible diffuse reflectance spectrum: Effects of aluminium substitution and grain morphology, *Clay Mineral.*, *46*, 137-147.

Liu, Q. S., V. Barrón, J. Torrent, S. G. Eeckhout, and C. Deng (2008), Magnetism of intermediate hydromaghemite in the transformation of 2-line ferrihydrite into hematite and its paleoenvironmental implications, *J. Geophys. Res.*, *113*, B01103, doi: 10.1029/2007jb005207.

Liu, Q. S., Y. B. Sun, X. K. Qiang, R. Tada, P. X. Hu, Z. Q. Duan, Z. X. Jiang, J. X. Liu, and K. Su (2015), Characterizing magnetic mineral assemblages of surface sediments from major Asian dust sources and implications for the Chinese loess magnetism, *Earth Planets Space*, *67*, 1-17.

Long, X., J. F. Ji, and W. Balsam (2011), Rainfall-dependent transformations of iron oxides in a tropical saprolite transect of Hainan Island, South China: Spectral and magnetic measurements, *J. Geophys. Res.*, *116*, F03015, doi:10.1029/2010JF001712.

Lyons, R., S. Tooth, and G. A. T. Duller (2014), Late Quaternary climatic changes revealed by luminescence dating, mineral magnetism and diffuse reflectance spectroscopy of river terrace palaeosols: A new form of geoproxy data for the southern African interior, *Quat. Sci. Rev.*, *95*, 43-59.

Maher, B. A., V. V. Karloukovski, and T. J. Mutch (2004), High-field remanence properties of synthetic and natural submicrometre haematites and goethites: Significance for environmental contexts, *Earth Planet. Sci. Lett.*, *226*, 491-505.

Malengreau, N., P. G. Weidler, and A. U. Gehring. (1997), Iron oxides in laterites - A combined mineralogical, magnetic, and diffuse reflectance study, *Schweiz. Mineral. Petrogr. Mitt.*, *77*, 13-20.

Mehra, O. P., and M. J. Jackson (1960), Iron oxide removal from soils and clays by a dithionite-citrate system buffered with sodium bicarbonate, *Clays. Clay. Mine*ral, *7*, 317-327.

Memon, M., K. S. Memon, M. S. Akhtar, and D. Stuben (2009), Characterization and quantification of iron oxides occurring in low concentration in soils, *Commun. Soil Sci. Plant Anal.*, *40*, 162-178.

Michel, F. M., V. Barrón, J. Torrent, M. P. Morales, C. J. Serna, J. F. Boily, Q. S. Liu, A. Ambrosini, A. C. Cismasu, and G. E. Brown (2010), Ordered ferrimagnetic form of ferrihydrite reveals links among structure, composition, and magnetism, *Proc. Natl. Acad. Sci. U.S.A.*, *107*, 2787-2792.

Özdemir, Ö., and D. J. Dunlop (2014), Hysteresis and coercivity of hematite, *J. Geophys. Res.*, *119*, 2582-2594.

Pollard, R. J., Q. A. Pankhurst, and P. Zientek (1991), Magnetism in aluminous goethite, *Phys. Chem. Mineral.*, *18*, 259-264.

Poulton, S. W., and D. E. Canfield (2005), Development of a sequential extraction procedure for iron: Implications for iron partitioning in continentally derived particulates, *Chem. Geol.*, *214*, 209-221.

Rochette, P., P. E. Mathé, L. Esteban, H. Rakoto, J. L. Bouchez, Q. S. Liu, and J. Torrent (2005), Non-saturation of the defect moment of goethite and fine-grained hematite up to 57 Teslas, *Geophys. Res. Lett.*, *32*, L22309, doi:10.1029/2005gl024196.

Scheinost, A. C., A. Chavernas, V. Barrón, and J. Torrent (1998), Use and limitations of second-derivative diffuse reflectance spectroscopy in the visible to near-infrared range to identify and quantify Fe oxide minerals in soils, *Clays Clay Miner.*, *46*, 528-536.

Scheinost, A. C., D. G. Schulze, and U. Schwertmann (1999), Diffuse reflectance spectra of Al substituted goethite: A ligand field approach, *Clays Clay Miner. 47*, 156-164.

Sellitto, V. M., R. B. A. Fernandes, V. Barrón, and C. Colombo (2009), Comparing two different spectroscopic techniques for the characterization of soil iron oxides: Diffuse versus bi-directional reflectance, *Geoderma*, *149*, 2-9.

Sherman, D. M., and T. D. Waite (1985), Electronic-spectra of Fe^{3+} oxides and oxide hydroxides in the near IR to near UV, *Am. Mineral.*, *70*, 1262-1269.

Stanjek, H., and U. Schwertmann (1992), The influence of aluminum on iron oxides. Part XVI, Hydroxyl and aluminum substitution in synthetic hematites, *Clays Clay Miner.*, *40*, 347-354.

Thompson, R., and F. Oldfield (1986), *Environmental Magnetism*, Allen and Unwin, London, 227 pp.

Torrent, J., and V. Barrón (2003), The visible diffuse reflectance spectrum in relation to the color and crystal properties of hematite, *Clays Clay Mineral.*, *51*, 309-317.

Torrent, J., and V. Barrón (2008), Diffuse reflectance spectroscopy, In: Dress, L. R., and A. L. Ulery (Eds.), Methods of Soil Analysis. Part 5. *Mineralogical Methods. Soil Science Society of America*, *pp. 367-387*.

Torrent, J., U. Schwertmann, and D. G. Schulze (1980), Iron oxide mineralogy of some soils of two river terrace sequences in Spain, *Geoderma*, *23*, 191-208.

Torrent, J., U. Schwertmann, H. Fechter, and F. Alferez (1983), Quantitative relationships between soil color and hematite content, *Soil Sci.*, *136*, 354-358.

Torrent, J., Q. S. Liu, J. Bloemendal, and V. Barrón (2007), Magnetic enhancement and iron oxides in the upper Luochuan loess-paleosol sequence, Chinese Loess Plateau, *Soil Sci. Soc. Am. J.*, *71*, 1570-1578.

Walker, T. R., E. E. Larson, and R. P. Hoblitt (1981), Nature and origin of hematite in the Moenkopi Formation (Triassic), Colorado Plateau: A contribution to the origin of magnetism in red beds, *J. Geophys. Res.*, *86*, 317-333.

Watari, F., P. Delavignette, J. Van Landuty, and S. Amelinckx (1983), Electron microscopic study of dehydration transformations. Part III: High resolution observation of the reaction process FeOOH → Fe_2O_3, *J. Solid State Chem.*, *48*, 49-64.

Wells, M. A., R. J. Gilkes, and R. R. Anand (1989), The formation of corundum and aluminous hematite by the dehydroxylation of aluminous goethite, *Clay Mineral.*, *24*, 513-530.

Wells, M. A., R. W. Fitzpatrick, R. J. Gilkes, and J. Dobson (1999), Magnetic properties of metal-substituted haematite, *Geophys. J. Int.*, *138*, 571-580.

Wiriyakitnateekul, W., A. Suddhiprakarn, I. Kheoruenromne, M. N. Smirk, and R. J. Gilkes (2007), Iron oxides in tropical soils on various parent materials, *Clay Mineral.*, *42*, 437-451.

Zhang, Y. G., J. F. Ji, W. L. Balsam, L. Liu, and J. Chen (2007), High resolution hematite and goethite records from ODP 1143, South China Sea: Co-evolution of monsoonal precipitation and El Niño over the past 600,000 years, *Earth Planet. Sci. Lett.*, *264*, 136-150.

Table and figure captions

Table 1 Synthesis routes and Al content of the studied hematite and goethite specimens.

Sample	Procedure and solution used	Aging temperature (°C)	Final Al content (mol%)
HFh0	100 mL 0.4 M $Fe(NO_3)_3$ + 1 M NaOH to pH=9 and L-tartrate 0.0008 M	95	0
HFh4	100 mL 0.384 M $Fe(NO_3)_3$ + 0.016 M $Al(NO_3)_3$ + 1 M NaOH to pH=9 and L-tartrate 0.0008 M	95	3.9
HFh8	100 mL 0.368 M $Fe(NO_3)_3$ + 0.032 M $Al(NO_3)_3$ + 1 M NaOH to pH=9 and L-tartrate 0.0008 M	95	6.8
HGL20	Goethite prepared oxidizing 1 L 0.04 M $FeSO_4$ + 0.01 M $Al(NO_3)_3$ + 110 mL 1 M $NaHCO_3$	800	15.8
HGL30	Goethite prepared oxidizing 1 L 0.035 M $FeSO_4$ + 0.015 M $Al(NO_3)_3$ + 110 mL 1 M $NaHCO_3$	800	26.6[1]
GT0	oxidizing 1 L 0.05 M $FeSO_4$ + 110 mL 1M $NaHCO_3$	20	0
GT8	oxidizing 1 L 0.046 M $FeSO_4$ + 0.004 M $Al(NO_3)_3$ +110 mL 1 M $NaHCO_3$	20	8.5
GT16	oxidizing 1 L 0.042 M $FeSO_4$ + 0.008 M $Al(NO_3)_3$ +110 mL 1 M $NaHCO_3$	20	15.3
GT20	oxidizing 1 L 0.04 M $FeSO_4$ + 0.01M $Al(NO_3)_3$ +110 mL 1 M $NaHCO_3$	20	17.9
GT30	oxidizing 1 L 0.034 M $FeSO_4$ + 0.016 M $Al(NO_3)_3$ +110 mL 1 M $NaHCO_3$	20	27.7

[1] Al content in the hematite crystals is likely < 16%.

Table 2 Particle size[2] and unit cell parameters[3] of the studied hematite and goethite specimens. The unit is nm.

		Particle size	a	b	c	d_{110}	d_{111}
Hematite	**HFh0**	167.2 ± 50	0.5042± 0.0004		1.3800 ± 0.0009	0.2522	
	HFh4	219.8 ± 66.6	0.5034± 0.0002		1.3766 ± 0.0005	0.2515	
	HFh8	358.1 ± 60.9	0.5033± 0.0007		1.3686 ± 0.0015	0.2526	
	HGL20	32.2 ± 7.2	0.5032± 0.0012		1.3682 ± 0.0026	0.2504	
	HGL30	20.8 ± 5.4	0.5017± 0.0009		1.3620 ± 0.0021	0.2496	
Goethite	**GT0**	Long axis: 349.5 ± 26.1 Short axis: 57.5 ± 4.9	0.4609 ± 0.0005	0.9986 ± 0.0006	0.3031 ± 0.0003		0.2460
	GT8	Long axis: 287.7 ± 43.3 Short axis: 64.9 ± 3.5	0.4612 ± 0.0005	0.9919 ± 0.0006	0.3021 ± 0.0002		0.2444
	GT16		0.4637 ± 0.0008	0.9861 ± 0.0012	0.3021 ± 0.0002		0.2439
	GT20		0.4635 ± 0.0005	0.9892 ± 0.0082	0.3034 ± 0.0024		0.2442
	GT30		0.4626 ± 0.0005	0.9952 ± 0.0005	0.3032 ± 0.0011		0.2442

[1] The mean grain size dimension of GT0 and GT8 is estimated at the 95% confidence level.
[2] d_{110} represents the d-values for the 110 line of hematite and d_{111} represents the d-values for the 111 line of goethite.

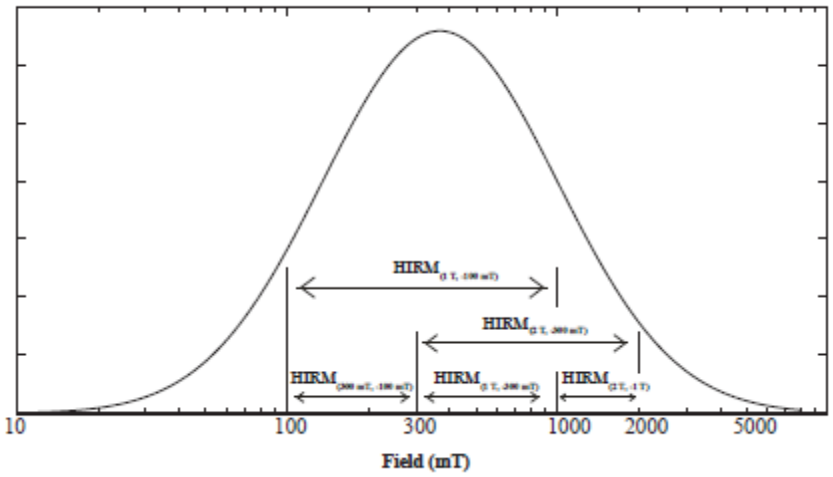

Figure 1 Schematic representation of the remanent coercivity fraction represented by $HIRM_{(FF, RF)}$. To simplify the illustration, it is assumed that the remanent coercivity of magnetic particles in natural samples follows a logarithmic Gaussian distribution; however, this is not an underlying assumption of the $HIRM_{(FF, RF)}$ approach.

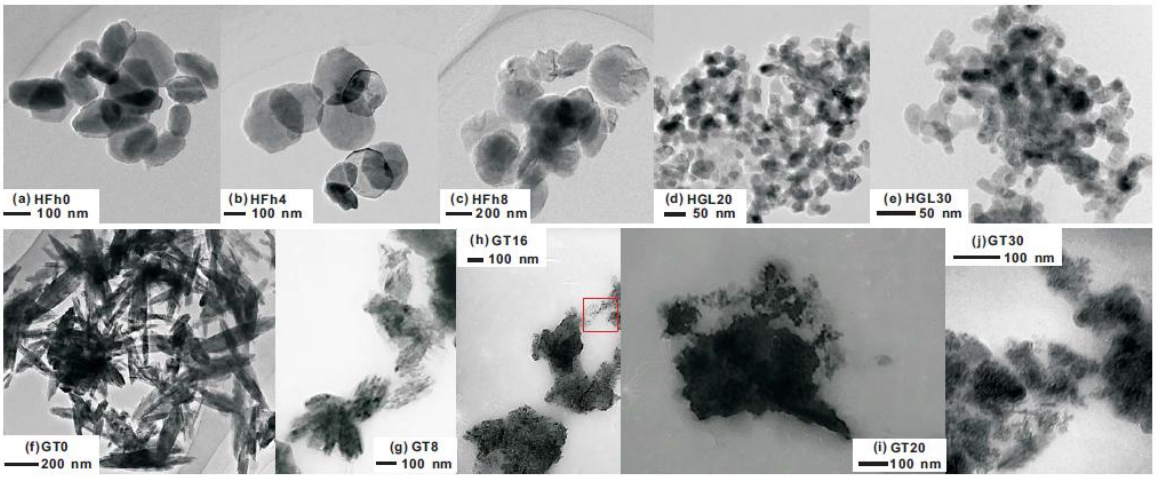

Figure 2 SEM and TEM images of the synthetic hematites and goethites analyzed in this study.

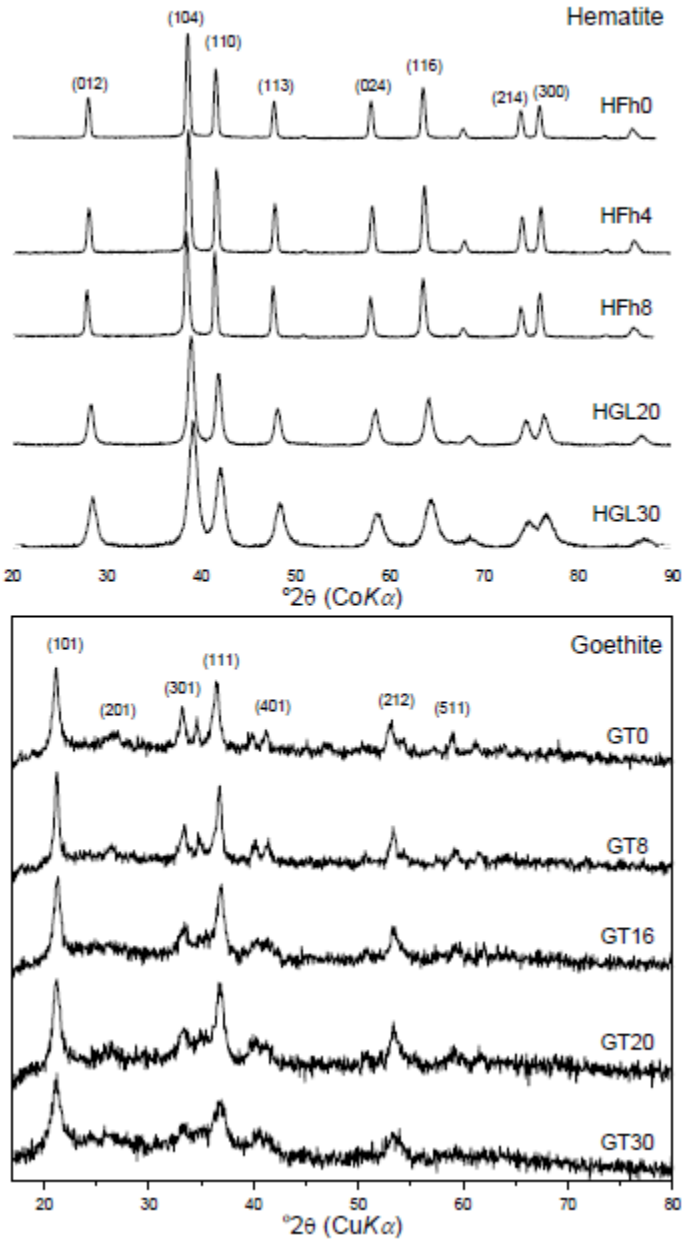

Figure 3 X-ray diffraction (XRD) spectra for synthetic hematite and goethite specimens. XRD data for HFh* samples are given by *Jiang et al.* [2012].

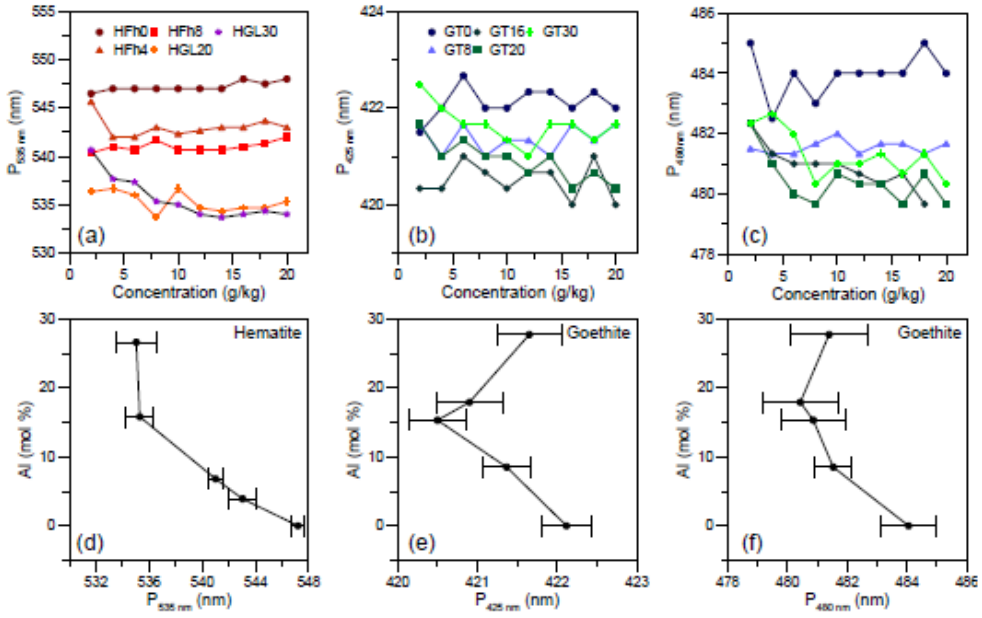

Figure 4 Variation in DRS band position for hematite ($P_{535\ nm}$) and goethite ($P_{425\ nm}$, $P_{480\ nm}$) with varying concentration of pure hematite and goethite (a, b, c) and levels of Al-substitution (d, e, f) in mixtures prepared with different concentrations. Error bars indicate the standard error of DRS band position among 10 subsamples with a single hematite or goethite.

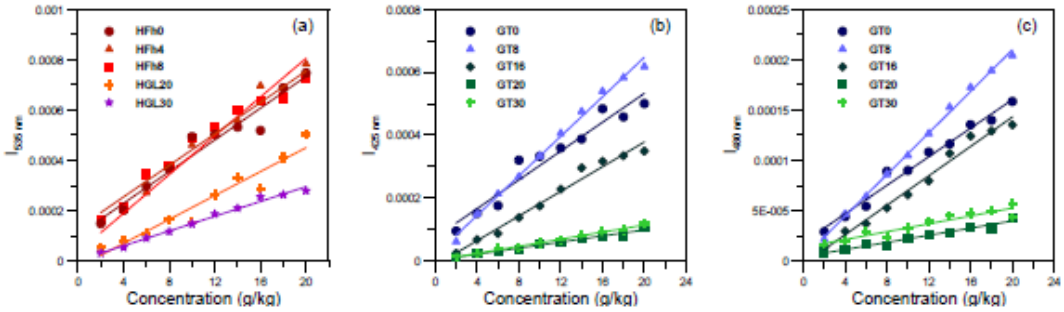

Figure 5 The relationship between (a) hematite and (b, c) goethite concentration with DRS second derivative intensity for mixture series with different levels of Al substitution.

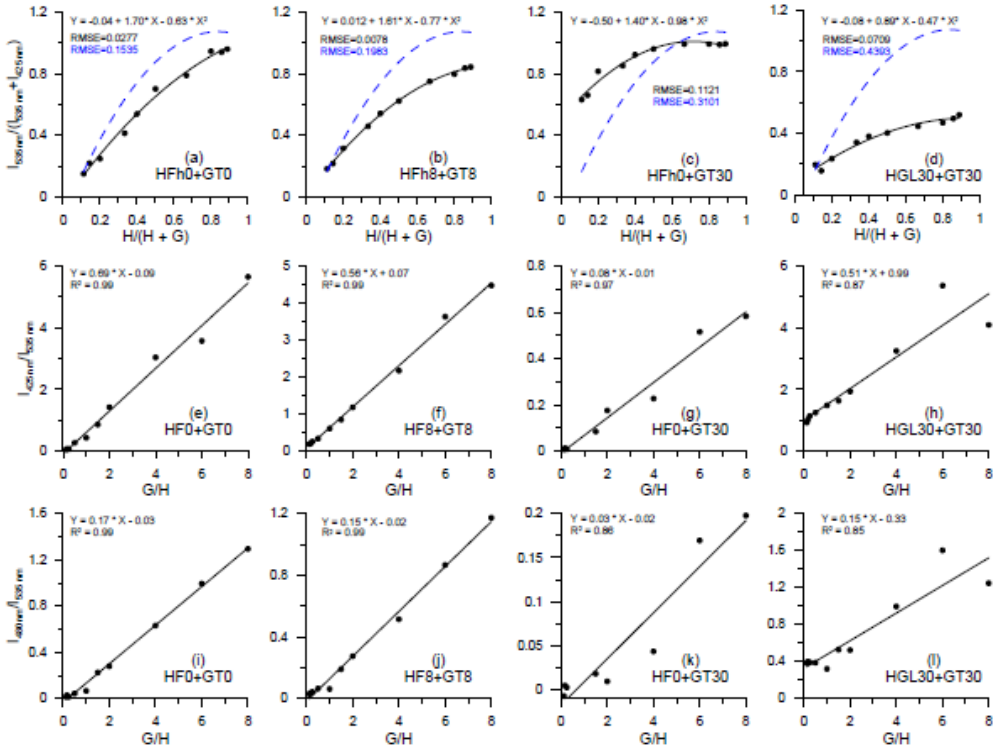

Figure 6 Empirical relationships between (a-d) DRS band intensity ratio $I_{535\ nm}/(I_{535\ nm} + I_{425\ nm})$ and concentration ratio H/(H + G); (e-h) $I_{425\ nm}/I_{535\ nm}$ and goethite/hematite concentration ratio G/H; (i-l) $I_{480\ nm}/I_{535\ nm}$ and goethite/hematite concentration ratio G/H. Blue dashed lines represent the regression function ($Y = -0.133+2.871\times X-1.709\times X^2$) from *Torrent et al*. [2007], where Y represents H/(H+G) and X represents $I_{535\ nm}/(I_{535\ nm} + I_{425\ nm})$. RMSE is the root mean square error of the polynomial fit.

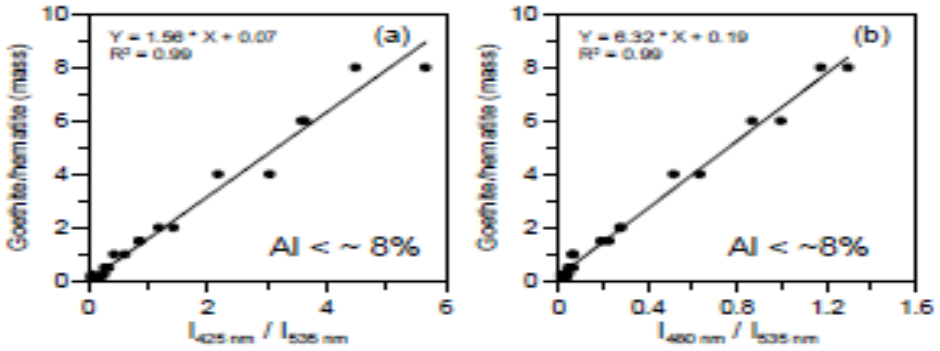

Figure 7 New transfer functions determined between DRS band intensity ratio. (a) $I_{425\ nm}/I_{535\ nm}$, (b) $I_{480\ nm}/I_{535\ nm}$, and goethite/hematite concentration ratio for samples with Al substitution below ~8%.

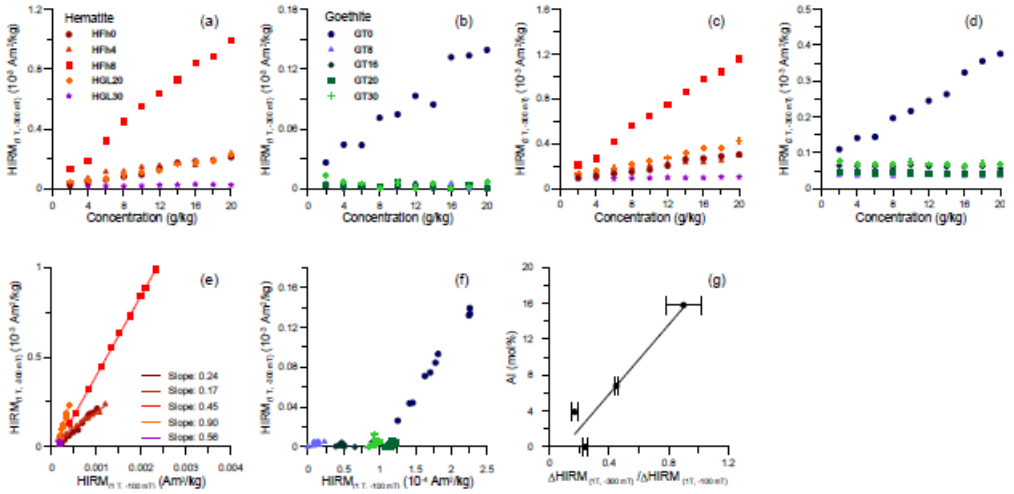

Figure 8 Plots of the relationship between (a, c) hematite and (b, d) goethite concentration and HIRM. Biplots of HIRM $_{(1\ T,\ -300\ mT)}$ and HIRM$_{(1T,\ -100\ mT)}$ for synthetic (e) hematite and (f) goethite. (g) ΔHIRM$_{(1\ T,\ -300\ mT)}$/ΔHIRM$_{(1\ T,\ -100\ mT)}$ ratio from (e) and its relationship with Al substitution. Errors on the ΔHIRM$_{(1\ T,\ -300\ mT)}$/ΔHIRM$_{(1\ T,\ -100\ mT)}$ ratio represent the 95% confidence intervals.

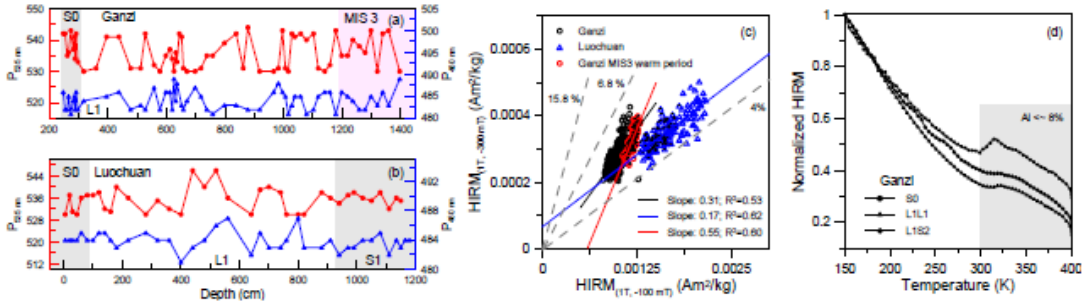

Figure 9 Variation of DRS hematite band position P_{535} (red line) and goethite band position $P_{480\ nm}$ (blue line) in the (a) Ganzi and (b) Luochuan loess sections. (c) Relationship between $HIRM_{(1T,\ -300\ mT)}$ and $HIRM_{(1\ T,\ -100\ mT)}$ for Ganzi (black circles), Luochuan (blue triangle) and the MIS3 warm period in the Ganzi section (red circles). Grey dashed lines mark the $\Delta HIRM_{(1T,\ -300\ mT)}/\Delta HIRM_{(1\ T,\ -100\ mT)}$ ratio for hematite with 4%, 6.8%, and 15.8% Al substitution based on Figure 8e, g. (d) $HIRM_{(1\ T,\ -300\ mT)}$ versus temperature curves for selected samples from the Ganzi section. The gray shaded area represents the T_b range of goethite with Al substitution < ~8%, based on the results of *Jiang et al.* [2014a].